PHYSICAL REVIEW RESEARCH **5**, L022043 (2023)

Letter

Optical dispersions through intracellular inhomogeneities

Masaki Watabe,[1,2,3,*] Yasuhiro Hirano,[4] Atsuko Iwane,[5] Osamu Matoba,[6] and Koichi Takahashi[1,7]
[1] *Laboratory for Biologically Inspired Computing, RIKEN Center for Biosystems Dynamics Research, Suita, Osaka 565-0874, Japan*
[2] *Cell Modeling and Simulation Group, Exploratory Research Center on Life and Living Systems, Okazaki, Aichi 444-8787, Japan*
[3] *Interdisciplinary Research Unit, National Institute of Basic Biology, Okazaki, Aichi 444-8585, Japan*
[4] *Nuclear Dynamics Group, Graduate School of Frontier Biosciences Osaka University, Suita, Osaka 565-0871, Japan*
[5] *Laboratory for Cell Field Structure, RIKEN Center for Biosystems Dynamics Research, Higashi-Hiroshima, Hiroshima 739-0046, Japan*
[6] *The Graduate School of System Informatics, Kobe University, Kobe, Hyogo 657-8501, Japan*
[7] *Institute for Advanced Bioscience, Keio University, Fujisawa, Kanagawa 252-8520, Japan*

(Received 13 July 2022; revised 19 July 2022; accepted 31 March 2023; published 30 May 2023)

The transport of intensity equation (TIE) exhibits a noninterferometric correlation between the intensity and phase variations of intermediate fields (e.g., light and electrons) in biological imaging. Previous TIE formulations have generally assumed free-space propagation of monochromatic, coherent field functions crossing phase distributions along a longitudinal direction. In this study, we modify the TIE with fractal (or self-similar) organization models based on intracellular refractive index turbulence. We then implement TIE simulations over a broad range of fractal dimensions and wavelengths. Simulation results show how the intensity propagation through the spatial fluctuation of intracellular refractive index interconnects fractal dimensionality with intensity dispersion (or transmissivity) within the picometer to micrometer wavelength range. Additionally, we provide a spatial autocorrelation of phase derivatives, which allows for the direct measurement and reconstruction of intracellular fractal profiles from optical and electron microscopy imaging.

DOI: 10.1103/PhysRevResearch.5.L022043

Introduction. Biological cells are the basic structural and functional unit of life. All cells consist of a cytoplasm enclosed within a membrane, which includes biomolecules (e.g., proteins and nucleic acids) and intracellular organelles (e.g., the endoplasmic reticulum, Golgi apparatus, and mitochondria). These complex intracellular structures can be visualized using optical imaging systems and electron microscopes. As visible light has a wavelength ranging from 360 to 760 nm, which is up to 5 orders of magnitude longer than the wavelength of electrons, optical imaging techniques tend to filter out the inner structures of smaller intracellular objects otherwise observable through electron microscopy.

The complex amplitude of a wave function describing optical fields is generally composed of two major physical quantities: amplitude and phase functions [1]. Variations in amplitudes (or intensities) can be captured directly by photosensitive detectors such as the human eye and scientific CMOS (complementary metal-oxide semiconductor) cameras. Variations in phases, however, are barely visible using optical microscopy systems and are sensitive to light scattering and fluctuations due to invisible spatial distributions of intracellular optical properties, e.g., refractive index and optical thickness. These phase variations have been formalized into a partial differential equation, termed the transport of intensity equation (TIE) [2–4], which is dependent on the wavelength and the intensity variations of intermediate fields (i.e., photon and electron). This equation represents, in particular, the free space propagation of a monochromatic coherent wave function to a given phase distribution along a longitudinal direction.

A key challenge to bridging the large resolution gap that lies between optical and electron microscopy techniques consists of finding meaningful variations in both intensity and phase functions. Over a broad range of wavelengths, the intensity and phase variations of intermediate fields are inextricably linked via the TIE. Previous TIE formalizations have generally assumed that a complex plane wave function describing intermediate fields can be propagated through an arbitrary phase distribution in free space. Intensity transport of the wave functions interacting with the complex refractive aspects of cellular interiors, however, remains elusive. In this Letter, we modify the TIE with fractal (or self-similar) organization models for intracellular refractive index turbulence. We then implement the TIE simulation in the picometer to micrometer wavelength range, computing intensity dispersions and reductions caused by inhomogeneous spatial distributions of the intracellular refractive index. Crucially, we show how the *a priori* lateral intensity distribution of a cell can be described as a function of its fractal dimensions. Such fractal media are optically thin and transparent through the visible wavelengths but exhibit the compression of fractal dimensionality and the increase of intensity dispersions in the wavelength range

---

[*] Corresponding author: m-watabe@nibb.ac.jp

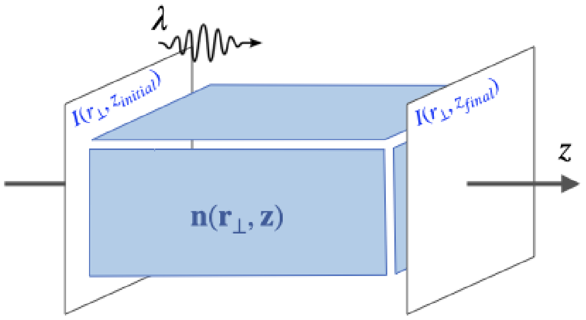

FIG. 1. For a given wavelength λ, the initial intensity distribution of a complex plane wave $I(r_\perp, z_{\text{initial}})$ propagates through the intracellular refractive index $n(r_\perp, z)$, exhibiting the final intensity distribution $I(r_\perp, z_{\text{final}})$.

of electron microscopy imaging. We also derive a spatial-autocorrelation function that interconnects phase derivatives with intracellular fractal profiles, and we demonstrate the direct measurements and reconstruction of optical properties from fluorescent cell imaging. Our work facilitates further extensions to bioimage simulation modules [5–14], incorporating, in particular, light scattering and fluctuations caused by nonuniform spatial distributions of intracellular optical properties. Such modification of the simulation is of particular relevance to the numerical evaluation and verification of observational invariance (or symmetry) as postulated in data science, likely leading to more realistic simulations of biological imaging.

Transport of intensity equation. For a specific intermediate field wavelength λ, the TIE can be formulated using the laws of conservation of energy (i.e., Helmholz equation) and parametrized with a complex refractive index for the intracellular media,

$$n(r_\perp, z) = n_0[1 + \Delta n(r_\perp, z) + i\kappa(r_\perp, z)], \tag{1}$$

where n_0 and $\Delta n(r_\perp, z)$ are the mean and spatial fluctuation of the refractive index, respectively. $\kappa(r_\perp, z)$ in the imaginary part denotes the spatial distribution of the attenuation index. In this formulation, a monochromatic coherent wave function propagating through the refractive index distribution along the axial axis (see Fig. 1) is given by

$$\psi(r_\perp, z) = A(r_\perp, z)e^{ikn_0 z}, \tag{2}$$

where $A(r_\perp, z)$ is the scalar complex amplitude of the wave function, and k is the wave number in free space $k = 2\pi/\lambda$. Substituting Eqs. (1) and (2) into the Helmholtz equation, we can deduce a paraxial wave equation,

$$\left[\nabla_\perp^2 + 2kn_0 i\frac{\partial}{\partial z} + 2kn_0\frac{\partial}{\partial z}(\beta + i\alpha)\right]A(r_\perp, z) = 0, \tag{3}$$

where $\nabla_\perp$ is the two-dimensional nabla operator in the transverse direction, i.e., $\nabla_\perp = (\partial/\partial x, \partial/\partial y)$. The α and β factors represent amplitude and phase variations arising from the spatial fluctuations of the refractive and attenuation indexes:

$$\alpha(r_\perp, z) = kn_0\int[1 + \Delta n(r_\perp, z)]\,\kappa(r_\perp, z)dz \tag{4}$$

and

$$\beta(r_\perp, z) = kn_0\int\left[\Delta n(r_\perp, z) - \frac{1}{2}\kappa(r_\perp, z)^2\right]dz. \tag{5}$$

Assuming the scalar complex amplitude of the paraxial wave function to be $A(r_\perp, z) = \sqrt{I(r_\perp, z)}e^{i\phi(r_\perp, z)}$, it is straightforward to derive a modified form of the TIE:

$$\begin{aligned}\frac{\partial I(r_\perp, z)}{\partial z} = &-\frac{1}{kn_0}\nabla_\perp\cdot[I(r_\perp, z)\nabla_\perp\phi(r_\perp, z)]\\ &-2\,\frac{\partial\alpha(r_\perp, z)}{\partial z}I(r_\perp, z),\end{aligned} \tag{6}$$

where $I(r_\perp, z)$ and $\phi(r_\perp, z)$ denote the intensity and the phase of the paraxial wave function. The β factor vanishes in the TIE modification but may be more relevant to phase changes in the transport of phase equation [3]. Furthermore, the derivation details are discussed in Sec. A.1 of the Supplemental Material (SM) [15].

The left-hand side of Eq. (6) represents the axial intensity differentiation that guides the intensity propagation along the z axis. The right-hand side of the equation exhibits the total energy variation in a lateral intensity distribution. Such energy variations are composed of two parts.

(i) The first part, $-\nabla_\perp\cdot[I\nabla_\perp\phi]/(kn_0)$, represents the intensity and phase variations arising from the spatial fluctuation of the refractive and attenuation index. There are two terms in these variations. $I\nabla_\perp^2\phi$ can be interpreted as the intensity fluctuation stemming from the convergent or divergent behavior of the intensity at the radius of the local phase curvature, the reciprocal of which is proportional to the Laplacian of the phase. $\nabla_\perp I\cdot\nabla_\perp\phi$ represents a measure of the translational effects of the phase gradient in the direction of the intensity gradient.

(ii) The second part, $-2(\partial\alpha/\partial z)I$, relates to Beer-Lambert's law of intensity reduction in an inhomogeneous medium, exhibiting, in particular, the energy absorption and scattering of the intermediate fields traveling through an intracellular medium.

Fractal cell modeling. A wave function of intermediate fields propagating through a biological medium can encounter structures with dimensions ranging from the size of a protein macromolecule (1–4 nm) and intracellular compartments: for example, membranes (10 nm), nucleus (5–10 μm), and mitochondria (0.2–2.0 μm). Cells also contain a cytoskeleton made of filaments (7–25 nm), as well as nucleoli (0.5–1.0 μm) and DNA in the form of chromatin in the nucleus. These complex structures are often modeled under the assumption that the constituents of cellular interiors are tightly filled with various discrete particles, with their surfaces pushed together to form contiguous biological components. Such cell modeling, when combined with Mie scattering theory, provides a homogeneous medium in a limited range of wavelengths and voxel size of the cell simulations [16–18]. Because of these constraints, the spatial fluctuations arising from the interactions between incoherent wave functions and discrete particles cannot be made to line up at the microscopic levels of intensity transport theory without breaking modeling assumptions.

Interactions of a wave function with intracellular inhomogeneities are associated with a turbulence in the refractive index distribution for which the spatial fluctuations are fractal

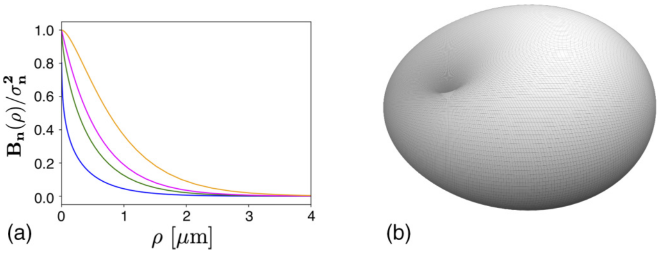

FIG. 2. Fractal model of intracellular refractive index turbulence. (a) The WM covariance as a function of distance between two different pixel positions ρ. Each colored line denotes one of the four representative models of fractal media: medium I (blue), medium II (green), medium III (magenta), and medium IV (orange). (b) An example of the mean differential scattering cross section per unit volume plotted in spherical coordinates ($l_c = 30$ nm). An incident wave function polarized in the vertical plane can propagate from left to right along the longitudinal direction. The dimple is located at the origin.

in nature [19–21]. For the sake of model simplicity, we consider intracellular constituents as a continuous fractal medium rather than the aggregation of various discrete particles. For a given fractal dimension D_f, which usually represents a mathematical index for characterizing fractal patterns or regularities by quantifying their complexity, continuous random fields of refractive index fluctuation Δn can be modeled by the Whittle-Matérn (WM) covariance (or correlation) function,

$$B_n(\rho) = \frac{\sigma_n^2 2^{1-\nu}}{|\Gamma(\nu)|}\left(\frac{\rho}{l_c}\right)^{\nu} K_\nu\left(\frac{\rho}{l_c}\right), \tag{7}$$

where l_c are σ_n^2 are the correlation length and the variance of the excessive refractive index, respectively. $K_\nu(\cdot)$ denotes the νth index of the modified Bessel function of the second kind $\nu = (D_f - 3)/2$. The shape of the WM covariance function can be exhibited in a wide range of plausible fractal dimensions including the power law for $D_f < 3$, Henyey-Greenstein for $D_f = 3$, the stretched exponential for $3 < D_f < 4$, Kolmogorov/von Karman for $D_f = 3.67$, the exponential for $D_f = 4$, and the Gaussian as $D_f \to \infty$. Figure 2(a) shows the WM covariance function for four different fractals models (see Sec. A.2.1 of the SM [15] for model parametrizations).

While the attenuation function in the fractal cell model can be represented by the intensity absorption coefficient μ_a and the scattering coefficient μ_s, most cells are transparent, weakly absorbing intermediate fields passing through their interiors. In a limiting case where $\mu_a \ll \mu_s$, we consider the four following assumptions: (i) the attenuation function is independent of the spatial variation of scattering coefficient, (ii) no backward scattering of the wave function, (ii) No depolarization effects, and (iv) the attenuation function can be written in the form

$$\kappa(r_\perp, z) = \frac{\langle \mu_s(kn_0)\rangle}{kn_0} = \frac{1}{kn_0}\iint_\Omega \left\langle \sigma\left(\hat{k}_o, \hat{k}_i\right)\right\rangle d\Omega, \tag{8}$$

where Ω and kn_0 are the solid angle and the effective wave number of intermediate fields, respectively. $\langle \mu_s(kn_0)\rangle$ represents the mean scattering coefficient derived from an integration of the mean differential scattering cross section $\langle \sigma(\hat{k}_o, \hat{k}_i)\rangle$ over all angles. Figure 2(b) shows an example of the scattering cross section in spherical coordinates, exhibiting, in particular, forward-directed scattering along the longitudinal direction (see Sec. A.2.2 of Ref. [15] for the σ definition and more figures for the four representative fractal media).

TIE simulations via fractal cell modeling. Fundamental characteristics of the intensity transport through continuous fractal media can be extracted from numerical simulations and analyses of the TIE. Here we assume that phase functions in the TIE are given by Eq. (5), i.e., $\phi(r_\perp, z) = -\beta(r_\perp, z)$, and we then implement TIE simulations over a wide range of fractal dimensions and wavelengths, computing the propagation and variation of the lateral intensity distribution through the fractal cell models along the axial direction (see Fig. 1). The finite difference approximation of the intensity propagation for the nth image frame can be represented in the form

$$\begin{aligned} I_{ij}^{n+1} &= I_{ij}^n + \delta z\left(\frac{\partial I}{\partial z}\right)_{ij}^n \\ &= I_{ij}^n + \delta z\left\{\frac{1}{kn_0}[\nabla_\perp \cdot (I\nabla_\perp\beta)] \right. \\ &\quad \left. - 2[1 + \Delta n(r_\perp, z)]\langle \mu_s(kn_0)\rangle I\right\}_{ij}^n, \end{aligned} \tag{9}$$

where i and j represent the index of the pixel position for a given image frame, with the convergence condition for TIE simulations being $\delta z < kn_0 \delta x \delta y$.

To analyze biophysical effects arising from intensity propagation via fractal cell modeling, we run the TIE simulations for the following two initial intensity conditions $I(r_\perp, z_{\text{initial}})$: a uniform intensity distribution 1000 counts/pixel, and a standard image in an intensity range from 500 to 1000 counts/pixel. Our simulation results for a thicker cell sample ($\sim$10 μm) are summarized in Fig. 3 (see Sec. B of the SM [15] for more simulation results. For $\lambda = 507$ nm, the intensity propagation of the standard image through the fractal medium III ($D_f = 4.00$) exhibits intensity attenuation and intensity dispersion in the final intensity image [see Fig. 3(b)]. Figure 3(d) shows a comparison between initial and final intensity histograms, thereby dispersing and reducing the intensity distribution of the initial standard image. However, for the fractal medium I ($D_f = 3.25$), there is significant transmissivity in the final intensity distribution [see Fig. 3(a)]; almost complete overlap between initial and final intensity histograms is shown in Fig. 3(a).

Convergence and stability of the TIE simulation can be seen in the size and the fractional error of the intensity dispersion which varies with axial distance. Figure 3(e) exhibits relatively fast convergence of the variation of root-mean-square (RMS) values along the axial direction ($z > 2$–3 μm). The TIE simulation for fractal medium I ($D_f = 3.25$) and medium II ($D_f = 3.67$) converges to steady state at relatively lower RMS values, roughly 50 (green line) and 11 (red line). However, at higher fractal dimensions, i.e., $D_f = 4.00$ and 5.00, the RMS value that gives rise to convergence of intensity dispersion is about 250 (magenta line) and 500 (orange line). In addition, Figure 3(f) shows propagation of averaged fractional

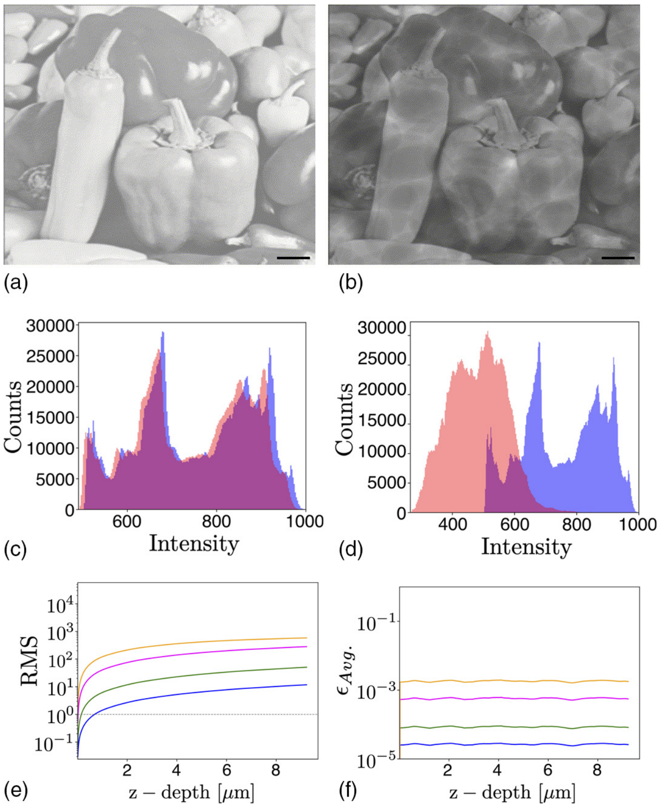

FIG. 3. The simulation results for thicker cell sample (∼10 μm). (a) Final intensity distribution for medium I ($D_f = 3.25$). Scale bar: 1.00 μm. (b) Final intensity distribution for medium III ($D_f = 4.00$). (c) Histogram comparison between initial and final intensity distributions for medium I ($D_f = 3.25$). Blue and red colored areas represent histograms for initial and final intensity distributions, respectively. (d) Comparison of intensity histograms for medium III ($D_f = 4.00$). (e) RMS variations arising from intensity propagation shown as a function of the z axis. Each colored line denotes one of the four different fractal models: medium I (blue), medium II (green), medium III (magenta), and medium IV (orange). (f) Averaged fractional errors shown as a function of the z axis.

errors along the z axis, $\epsilon(z_p)=|I(z_p)-I(z_{p-1})|/I(z_p)$, thus implying no divergence of numerical errors.

Electron microscopy is capable of imaging thinner cell sample sizes less than 150 nm [22]. In the wavelength range of electron beams, we consider optical depth (or thickness) to quantify a specific level of transparency of the four fractal media. Optical depth is a dimensionless factor that generally represents a measure of scattering and absorption up to a specific "depth" of intracellular media when intermediate fields (e.g., light and electron) travel through the structure inside the sample. In fractal cell modeling, optical depth can be defined as follows:

$$\tau = \int_0^L \langle \mu_s(kn_0) \rangle dz, \tag{10}$$

where L is the physical thickness of biological samples. For $L = 110$ nm, Figure 4 shows the optical depth over a broad range of wavelengths from electron beams (blue region, $\lambda =$ 1.00 pm to 1.00 nm) to visible light (green region, $\lambda =$ 360–760 nm). The fractal media are optically thin ($\tau \ll 1$) and transparent through the visible light wavelength, weakly dispersing the light intensities passing through their interiors. Such intensity dispersion thus provides approximately invariant transport between initial and final intensity distributions, $I(z_{\mathrm{final}}) \sim I(z_{\mathrm{initial}})$ (see Fig. S10(a) in Sec. B2 of the SM [15]). However, in a wavelength range of electron microscopy imaging, there is a significant tradeoff between fractal dimensionality and optical depth. Fractal medium I (blue), medium II (green), and medium III (magenta) are optically thick ($\tau \gg 1$), exhibiting, in particular, intensity attenuation as well as intensity dispersion in the final standard image (see Figs. S10(d)–S10(f) of Ref. [15]). Mathematically speaking, as the fractal dimensions increase, the optical depth becomes thinner and the transmissivity thereof can be increased in fractal medium IV (orange).

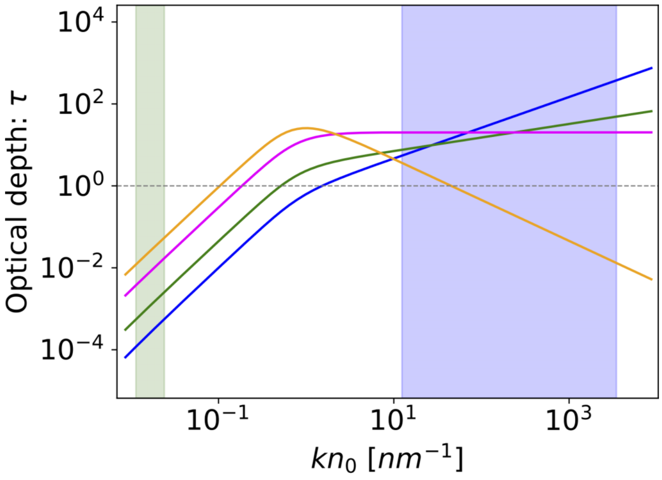

FIG. 4. Optical depth for sample thickness ($L = 110$ nm) represented over a wide range of effective wave number kn_0 values, from visible light (green) to electron beam (blue). Color lines denote the four different fractal media. If $\tau \gg 1$, then the sample is optically thick. If $\tau \ll 1$, then the sample is optically thin. The dashed line represents $\tau = 1$.

Application. A further motivation for our work is the direct measurement and reconstruction of the refractive index profiles of cellular interiors. Recent experimental studies using the TIE via bioimaging [4,23], for example, have reconstructed intracellular phase distributions without modeling the refractive index turbulence. Likewise, Rogers and his colleagues have verified the apparent similarity in power spectral densities between the WM covariance function and scanning electron microscopy images [20]. These qualitative verifications, however, were made without applying intensity transport theory and so cannot be valid as direct measurements of the refractive index profiles. For a proper comparison and measurement in bioimaging, a mathematical relation between the phase factor and the WM covariance model can be derived from the spatial autocorrelation of Eq. (5) and then written in the form

$$\left\langle \frac{\partial \beta(r)}{\partial z} \frac{\partial \beta(r+\rho)}{\partial z} \right\rangle = (kn_0)^2 B_n(\rho) + \left[\frac{\langle \mu_s(kn_0) \rangle}{\sqrt{2kn_0}} \right]^4 \tag{11}$$

when satisfying the four assumptions declared in the cell modeling section (see Sec. C.1 of the SM [15] for derivation details). In this formula, the WM covariance function $B_n(\rho)$ and the mean scattering coefficient $\langle\mu(kn_0)\rangle$ represent the shape and offset of the phase-differential autocorrelation along axial directions. Figure S11 of Ref. [15] shows no significant shape differences over a broad wavelength range from electron beams (dashed lines) to visible lights (solid lines); a large variation of the offset is found at $\rho > 10$ μm due to the dependence on the effective wave number. Moreover, we use this mathematical relation to reconstruct intracellular optical properties (e.g., fractal dimension and scattering coefficient) from fluorescent cell imaging. In our demonstration, the covariance function is directly compared and fitted to the observed spatial-autocorrelation curves of phase derivatives. Table S4 and Fig. S14 of Ref. [15] not only represent the best estimates in fractal model parameters but also their statistical uncertainties which give a numerical indication of the level of validity and confidence in our fitting results (see Sec. C.2 of the SM [15] for analysis details; see also Refs. [3,4,24–33]).

Conclusion. The TIE plays a key role in bridging the resolution gap between optical and electron microscopy techniques, providing, in particular, a noninterferometric correlation between intensity and phase functions of intermediate fields (e.g., electrons and light) over a broad range of wavelengths. These microscopy techniques are capable of directly imaging the intensity variations of intermediate fields passing through the interior of cells. Variations in phases, however, are barely visible with bioimaging systems and are sensitive to light scattering and fluctuation through invisible (or unobservable) spatial distributions of intracellular refractive and attenuation indexes. In this paper, we reformulated the TIE through fractal modeling of these two indexes. Our results from these TIE simulations revealed that intensity propagations through the refractive index fluctuation can lead to nonintuitive interconnections of fractal dimensionality and intensity dispersion (or transmissivity) in the picometer to micrometer wavelength range. We also derived the spatial correlation of phase derivatives that enables the direct measurements of the WM covariance model parameters from optical and electron microscopy imaging.

Of further significance to our work is a numerical evaluation and verification of observational invariance (or symmetry) as postulated in data science. Most subcellular observations made via optical imaging are dedicated to an empirical (or data-driven) approach, its main function being to allow biophysicists to extract the regularities and patterns of the apparent intracellular properties captured with photosensitive devices [34–38]. These regularities are often formalized into network models, mainly as a function of the observable intracellular components. However, in actual intracellular imaging, propagations and variations of light through inhomogeneous intracellular structures are dependent on the wavelength of light, as well as intracellular optical properties such as the refractive index, optical thickness, and attenuation coefficients. These optical dependencies raise questions regarding whether the subcellular model representations can be conserved or violated through observational processes. Our work sheds light on these questions from the perspective of fundamental optics and also suggests new developments and extensions to bioimage simulation modules [5–14], including, in particular, light scattering and fluctuations caused by the nonuniform spatial distributions of intracellular optical properties. Such an implementation is of broad relevance beyond just the TIE simulations presented here and will likely lead to more realistic simulations of biological imaging.

We would like to thank Hideaki Yoshimura, Takahiro Nishimura, Naru Yoneda, Kazunari Kaizu, Kozo Nishida, and all the other members of the laboratory for biologically inspired computing at RIKEN for their guidance and support throughout this research work. The research work is supported by JSPS (Japanese Society for the Promotion of Science) KAKENHI Grants No. JP20H05886, No. JP20H05891, No. JP20K21836 and No. JP21H05605.

---

[1] M. Born and E. Wolf, *Principles of Optics: Electromagnetic Theory of Propagation, Interference and Diffraction of Light*, 7th ed. (Cambridge University, Cambridge, England).

[2] M. R. Teague, Deterministic phase retrieval: A Green's function solution, J. Opt. Soc. Am. **73**, 1434 (1983).

[3] C. Zuo, J. Li, J. Sun, Y. Fan, J. Zhang, L. Lu, R. Zhang, B. Wang, L. Huang, and Q. Chen, Transport of intensity equation: A tutorial, Opt. Lasers Eng. **135**, 106187 (2020).

[4] M. Mitome, Transport of intensity equation method and its applications, Microscopy **70**, 69 (2021).

[5] S. Mahajan and T. Tang, Meeting experiments at the diffraction barrier with in silico fluorescence microscopy, ACS Photonics **9**, 846 (2022).

[6] M. Weigert, K. Subramanian, S. T. Bundschuh, W. Myers, and M. Kreysing, Biobeam—Multiplexed wave-optical simulations of light-sheet microscopy, PLoS Comput. Biol. **14**, e1006079 (2018).

[7] A. Girsault, T. Lukes, A. Sharipov, S. Geissbuehler, M. Leutenegger, W. Vandenberg, P. Dedecker, J. Hofkens, and T. Lasser, SOFI simulation tool: A software package for simulating and testing super-resolution optical fluctuation imaging, PLoS ONE **11**, e0161602 (2016).

[8] M. Lindén, V. Ćurić, A. Boucharin, D. Fange, and J. Elf, Simulated single molecule microscopy with SMeagol, Bioinformatics **32**, 2394 (2016); M. Lindén, V. Ćurić, E. Amselem, and J. Elf, Pointwise error estimates in localization microscopy, Nat. Commun. **8**, 1 (2017).

[9] V. Venkataramani, F. Herrmannsdörfer, M. Heilemann, and T. Kuner, SuReSim: simulating localization microscopy experiments from ground truth models, Nat. Methods **13**, 319 (2016).

[10] M. Watabe, S. N. V. Arjunan, W. X. Chew, K. Kaizu, and K. Takahashi, Simulation of live-cell imaging system reveals hidden uncertainties in cooperative binding measurements, Phys. Rev. E **100**, 010402(R) (2019); M. Watabe, S. N. V. Arjunan, S. Fukushima, K. Iwamoto, J. Kozuka, S. Matsuoka, Y. Shindo, M. Ueda, and K. Takahashi, A computational framework for bioimaging simulation, PLoS ONE **10**, e0130089 (2015).

[11] J. Angiolini, N. Plachta, E. Mocskos, and V. Levi, Exploring the dynamics of cell processes through simulations of fluorescence microscopy experiments, Biophys. J. **108**, 2613 (2015).

[12] S. H. Rezatofighi, W. T. E. Pitkeathly, S. Gould, R. Hartley, K. Mele, W. E. Hughes, and J. G. Burchfield, A framework for generating realistic synthetic sequences of total internal reflection fluorescence microscopy images, in *Proceedings of the IEEE 10th International Symposium on Biomedical Imaging* (IEEE, New York, 2013), pp. 157–160.

[13] I. F. Sbalzarini, Modeling and simulation of biological systems from image data, BioEssays **35**, 482 (2013).

[14] J. Boulanger, C. Kervrann, and P. Bouthemy, A simulation and estimation framework for intracellular dynamics and trafficking in video-microscopy and fluorescence imagery, Med. Image Anal. **13**, 132 (2009).

[15] See Supplemental Material at http://link.aps.org/supplemental/10.1103/PhysRevResearch.5.L022043 for further details.

[16] J. M. Schmitt and G. Kumar, Optical scattering properties of soft tissue: a discrete particle model, Appl. Opt. **37**, 2788 (1998).

[17] K. Kaizu, K. Nishida, Y. Sakamoto, S. Kato, T. Niina, N. Nishida, N. Aota, M. Koizumi, and K. Takahashi, E-Cell System Version 4, doi: 10.5281/zenodo.3365597 (2019).

[18] W. X. Chew, K. Kaizu, M. Watabe, S. V. Muniandy, K. Takahashi, and S. N. V. Arjunan, Surface reaction-diffusion kinetics on lattice at the microscopic scale, Phys. Rev. E **99**, 042411 (2019); W.-x. Chew, K. Kaizu, M. Watabe, S. V. Muniandy, K. Takahashi, and S. N. V. Arjunan, Reaction-diffusion kinetics on lattice at the microscopic scale, *ibid.* **98**, 032418 (2018); S. N. V. Arjunan and M. Tomita, A new multicompartmental reaction-diffusion modeling method links transient membrane attachment of *E. coli* MinE to E-ring formation, Syst. Synth. Biol. **4**, 35 (2010).

[19] A. K. Glaser, Y. Chen, and J. T. C. Liu, Fractal propagation method enables realistic optical microscopy simulations in biological tissues, Optica **3**, 861 (2016).

[20] J. D. Rogers, A. J. Radosevich, J. Yi, and V. Backman, Modeling light scattering in tissue as continuous random media using a versatile refractive index correlation function, IEEE J. Sel. Top. Quantum Electron. **20**, 1 (2013).

[21] A. Wax and V. Backman, *Biomedical Applications of Light Scattering* (McGraw–Hill, New York, 2010), p. 401; J. D. Rogers, I. R. Capoglu, and V. Backman, Nonscalar elastic light scattering from continuous media in the Born approximation: Erratum, Opt. Lett. **35**, 1367 (2010).

[22] Electron microscopy, TEM vs SEM, Thermo Fisher Scientific, https://www.thermofisher.com/jp/ja/home/materials-science/learning-center/applications/sem-tem-difference.html, accessed: 2022-12-27.

[23] S. K. Rajput, O. Matoba, M. Kumar, X. Quan, Y. Awatsuji, Y. Tamada, and E. Tajahuerce, Multi-physical parameter cross-sectional imaging of quantitative phase and fluorescence by integrated multimodal microscopy, IEEE J. Sel. Top. Quantum Electron. **27**, 6801809 (2021).

[24] N. Yudistira, M. Kavitha, T. Itabashi, A. H. Iwane, and T. Kurita, Prediction of sequential organelles localization under imbalance using a balanced deep U-net, Sci. Rep. **10**, 2626 (2020).

[25] T. M. Ichinose and A. H. Iwane, Cytological analyses by advanced electron microscopy, in *Cyanidioschyzon merolae*, edited by T. Kuroiwa, S. Miyagishima, S. Matsunaga, N. Sato, H. Nozaki, K. Tanaka, and O. Misumi (Springer, Berlin, 2017), pp. 129–151.

[26] S. Y. Miyagishima and K. Tanaka, The unicellular red alga *Cyanidioschyzon merolae*—The simplest model of a photosynthetic eukaryote, Plant and Cell Physiology **62**, 926 (2021).

[27] S. van der Walt, J. L. Schönberger, J. Nunez-Iglesias, F. Boulogne, J. D. Warner, N. Yager, E. Gouillart, T. Yu, and the scikit-image contributors, scikit-image: Image processing in Python, PeerJ **2**, e453 (2014).

[28] S. Müller, L. Schüler, A. Zech, and F. Heße, `GSTools` v1.3: A toolbox for geostatistical modelling in python, Geosci. Model Dev. **15**, 3161 (2022).

[29] H. Kimura, N. Takizawa, E. Allemand, T. Hori, F. J. Iborra, N. Nozaki, M. Muraki, M. Hagiwara, A. R. Krainer, T. Fukagawa, and K. Okawa, A novel histone exchange factor, protein phosphatase 2Cγ, mediates the exchange and dephosphorylation of H2A-H2B, J. Cell Biol. **175**, 389 (2006).

[30] M. Watabe, Physical constraints to phase retrieval using the transport of intensity equation in fluorescence microscopy imaging, presented at the 1st Conference for Sensing and Imaging Through Scattering and Fluctuating Field in Biology, Telecommunication and Astronomy (SI-Thru2022), April 19–22, 2022, at Pacifico Yokohama, Japan.

[31] S. Mazumder, *Numerical Methods for Partial Differential Equations: Finite Difference and Finite Volume Methods*, 1st ed. (Academic Press, San Diego, 2016).

[32] B. Xue and S. Zheng, Phase retrieval using the transport of intensity equation solved by the FMG-CG method, Optik **122**, 2101 (2011).

[33] S. V. Pinhasi, R. Alimi, L. Perelmutter, and S. Eliezer, Topography retrieval using different solutions of the transport intensity equation, J. Opt. Soc. Am. A **27**, 2285 (2010).

[34] E. Meijering, A bird's-eye view of deep learning in bioimage analysis, Comput. Struct. Biotechnol. J. **18**, 2312 (2020).

[35] E. Moen, D. Bannon, T. Kudo, W. Graf, M. Covert, and D. Van Valen, Deep learning for cellular image analysis, Nat. Methods **16**, 1233 (2019).

[36] M. I. Jordan and T. M. Mitchell, Machine learning: Trends, perspectives, and prospects, Science **349**, 255 (2015).

[37] V. Marx, The big challenges of big data, Nature (London) **498**, 255 (2013).

[38] G. Danuser, Computer vision in cell biology, Cell **147**, 973 (2011).